

Broad-line region structure and kinematics in the radio galaxy 3C 120^{★,★★}

W. Kollatschny¹, K. Ulbrich¹, M. Zetzl¹, S. Kaspi^{2,3}, and M. Haas⁴

¹ Institut für Astrophysik, Universität Göttingen, Friedrich-Hund Platz 1, 37077 Göttingen, Germany
e-mail: wkollat@astro.physik.uni-goettingen.de

² School of Physics & Astronomy and the Wise Observatory, The Raymond and Beverly Sackler Faculty of Exact Sciences, Tel-Aviv University, 69978 Tel-Aviv, Israel

³ Physics Department, Technion, 32000 Haifa, Israel

⁴ Astronomisches Institut, Ruhr-Universität Bochum, Universitätsstrasse 150, 44801 Bochum, Germany

Received 28 March 2014 / Accepted 29 April 2014

ABSTRACT

Context. Broad emission lines originate in the surroundings of supermassive black holes in the centers of active galactic nuclei (AGN). These broad-line emitting regions are spatially unresolved even for the nearest AGN. The origin and geometry of broad-line region (BLR) gas and their connection with geometrically thin or thick accretion disks is of fundamental importance for the understanding of AGN activity.

Aims. One method to investigate the extent, structure, and kinematics of the BLR is to study the continuum and line profile variability in AGN. We selected the radio-loud Seyfert 1 galaxy 3C 120 as a target for this study.

Methods. We took spectra with a high signal-to-noise ratio of 3C 120 with the 9.2 m Hobby-Eberly Telescope between Sept. 2008 and March 2009. In parallel, we photometrically monitored the continuum flux at the Wise observatory. We analyzed the continuum and line profile variations in detail (1D and 2D reverberation mapping) and modeled the geometry of the line-emitting regions based on the line profiles.

Results. We show that the BLR in 3C 120 is stratified with respect to the distance of the line-emitting regions from the center with respect to the line widths (FWHM) of the rms profiles and with respect to the variability amplitude of the emission lines. The emission line wings of H α and H β respond much faster than their central region. This is explained by accretion disk models. In addition, these lines show a stronger response in the red wings. However, the velocity-delay maps of the helium lines show a stronger response in the blue wing. Furthermore, the He II λ 4686 line responds faster in the blue wing in contradiction to observations made one and a half years later when the galaxy was in a lower state. The faster response in the blue wing is an indication for central outflow motions when this galaxy was in a bright state during our observations. The vertical BLR structure in 3C 120 coincides with that of other AGN. We confirm the general trend: the emission lines of narrow line AGN originate at larger distances from the midplane than AGN with broader emission lines.

Key words. galaxies: active – galaxies: Seyfert – galaxies: nuclei – galaxies: individual: 3C 120 – quasars: emission lines

1. Introduction

The variable radio source 3C 120 has been identified to be a distant Seyfert 1 galaxy of redshift 0.0334 by Burbidge (1967) as early as 1967. Later on, French & Miller (1980) and Oke et al. (1980) observed short-term variations (i.e. within of one year) and long-term spectral variations in the continuum and in the broad emission lines during an observing period from 1967 to 1980. Peterson et al. (1998) carried out a spectral variability campaign of 3C 120 during a period of eight years from 1989 to 1996. They derived a delay of $\tau = 44.{}^{+28}_{-20}$ days of the integrated H β emission line with respect to the variable continuum flux. The value of this delay – that is the distance of the line-emitting region from the central ionizing source – had a large

error because the continuum and emission-line light curves were not sampled densely. Their mean and median sampling rate was 50 and 11 days, respectively.

We carried out an additional spectral variability campaign of 3C 120 with the 9.2 m Hobby-Eberly Telescope (HET) in the years 2008 and 2009 to study in detail variations in the integrated line fluxes and in the profiles of the optical Balmer and helium lines. The study of variations in emission-line profiles of active galactic nuclei (AGN) contains information about the structure and kinematics of the central line-emitting regions in Seyfert 1 galaxies in combination with model calculations. Relative variations in individual segments of emission lines with respect to each other were verified before, for instance, in variability campaigns of the UV C IV λ 1550 line in NGC 4151, NGC 5548 (Gaskell 1988; Korista et al. 1995) or in the Balmer lines of NGC 5548, NGC 4593 (Kollatschny & Dietrich 1996, 1997). There have been indications of a shorter delay in the red line wings than in the blue wings in all these variability campaigns. Detailed two-dimensional (2D) reverberation-mapping studies have been carried out so far only for a few galaxies (Kollatschny 2003; Bentz et al. 2010; Grier et al. 2013). Grier et al. (2013)

* Based on observations obtained with the Hobby-Eberly Telescope, which is a joint project of the University of Texas at Austin, the Pennsylvania State University, Stanford University, the Ludwig-Maximilians-Universität München, and the Georg-August-Universität Göttingen.

** Tables 1, 2, 4, 5 are available in electronic form at <http://www.aanda.org>

monitored three spectral lines of 3C 120 in the year 2010 when this galaxy was in a low state. We compare their findings with the results of our variability campaign.

Line profile studies confirmed the general picture that the broad-line emitting region (BLR) is gravitationally bound and that the emission lines originate in flattened accretion disk structures with additional indications of inflow or outflow motions. The analyses of the integrated line-intensity variations and their line profile variations are important tools for studying the central BLR in AGN. In addition, the line profiles – that is, their observed full-width at half maximum line values (FWHM) and σ_{line} values – contain information on the rotational and turbulent velocities in the line-emitting regions above the accretion disk (Kollatschny & Zetzl 2011, 2013a,b,c). Based on these velocity studies, we were able to determine the heights of the line-emitting regions above the midplane in combination with the line-emitting distances from the ionizing central source for a few active galaxies. Here we present additional information regarding the vertical BLR structure in 3C 120 by modeling their line profiles, as we have done before for four other Seyfert galaxies (Kollatschny & Zetzl 2013b,c), and we compare the BLR structures with each other.

The paper is arranged in the following way: in Sect. 2 we describe the observations taken with the HET Telescope. In Sect. 3 we present our data analysis and results on the structure and kinematics of the central BLR in 3C 120. In Sect. 4 we discuss the results of our variability campaign compared with other campaigns of this galaxy. Finally, we analyze the BLR structure in this galaxy and compare it with that of other Seyfert galaxies. A short summary is given in Sect. 5.

2. Observations and data reduction

We took optical spectra of the AGN in the Seyfert galaxy 3C 120 with the HET telescope at McDonald Observatory at 31 epochs between September 17, 2008, and March 16, 2009. The log of our spectroscopic observations is given in Table 1.

The obtained spectra span a period of 179.7 days. The median interval between the individual observations was 4.1 days and the average interval was 5.8. During the first two months of our campaign we took 19 spectra with an average interval of 3.5 days. In some cases we acquired spectra at intervals of only one day.

All spectroscopic observations were performed under identical instrumental conditions with the Marcario Low Resolution Spectrograph (LRS) mounted at the prime focus of HET. The detector was a 3072×1024 $15 \mu\text{m}$ pixel Ford Aerospace CCD with 2×2 binning. The spectra cover the wavelength range from 4200 Å to 6900 Å (LRS grism 2 configuration) in the rest frame of the galaxy with a resolving power of 650 at 5000 Å (7.7 Å FWHM). All observations were taken with exposure times of 10 to 20 min, which in most cases yielded a signal-to-noise ratio of at least 100 per pixel in the continuum. The slit width was fixed to $2''.0$ projected on the sky at an optimized position angle to minimize differential refraction. Furthermore, all observations were taken at the same airmass thanks to the particular design feature of the HET. We extracted seven columns from each of our object spectra, corresponding to $3''.3$. The spatial resolution was $0''.472$ per binned pixel.

Both HgCdZn and Ne spectra were taken after each object exposure to enable the wavelength calibration. Spectra of different standard stars were observed for flux calibration as well.

The reduction of the spectra (bias subtraction, cosmic ray correction, flat-field correction, 2D-wavelength calibration,

night-sky subtraction, and flux calibration) was made in a homogeneous way with IRAF reduction packages (Kollatschny et al. 2001). The spectra were not corrected for the variable atmospheric absorption in the *B* band.

Great care was taken to ensure high-quality intensity and wavelength calibrations to keep the intrinsic measurement errors very low (Kollatschny et al. 2001, 2003, 2010). Our galaxy spectra as well as our calibration star spectra were not always taken under photometric conditions. Therefore, all spectra were calibrated to the same absolute [O III] $\lambda 5007$ flux of $3.02 \times 10^{-13} \text{ erg s}^{-1} \text{ cm}^{-2}$ (taken from Peterson et al. 1998). The flux of the narrow emission line [O III] $\lambda 5007$ is considered to be constant on time scales ranging from one to a few years (Peterson et al. 2013).

The accuracy of the [O III] $\lambda 5007$ flux calibration was tested for all forbidden emission lines in the spectra. We calculated difference spectra for all epochs with respect to the mean spectrum of our variability campaign. Corrections for both small spectral shifts ($<0.5 \text{ \AA}$) and small scaling factors were executed by minimizing the residuals of the narrow emission lines in the difference spectra. All wavelengths were converted to the rest frame of the galaxy ($z = 0.03302$). Throughout this paper, we assume that $H_0 = 70 \text{ km s}^{-1} \text{ Mpc}^{-1}$. A relative flux accuracy on the order of 1% was achieved for most of our spectra.

In addition to our spectra of 3C 120 taken with the HET (H) we obtained photometric data taken with the 1m telescope at the Wise observatory (W) of the Tel-Aviv University in Israel. The 1m telescope is equipped with the 1340×1300 pixels PI-CCD camera which has a $13' \times 13'$ field of view with a scale of 0.58 arcsec/pix . Observations were carried out in Bessel *V* and *R* bands with exposure times of 5 min. The images were reduced in the standard way using IRAF routines. Broad-band light curves were produced by comparing their instrumental magnitudes with those of non-variable stars in the field (see, e.g., Netzer et al. 1996, for more details). The quoted uncertainties on the photometric measurements include the fluctuations due to photon statistics and the scatter in the measurement of the non-variable stars used.

During November and December 2008, *I'*-band measurements were taken with the 40 cm monitoring telescope of the Universitätssternwarte Bochum near Cerro Armazones in Chile (Ramolla et al. 2013). The filter *I'* is the *i*-band of PANSTARRS, similar to SLOAN *i*. This filter is centered on 7700 Å with a width of 1500 Å. Per night, ten dithered 60 s exposures with a size of $27' \times 41'$ were reduced in a standard manner and then combined. Light curves were extracted using $15''$ apertures and five non-variable stars on the same images and of similar brightness as 3C 120. A list of the photometric observations is given in Table 2.

3. Results and discussion

3.1. Continuum and spectral line variations

We present in Fig. 1 all reduced optical spectra of 3C 120 that were taken during our variability campaign. All 31 spectra are shown in the rest frame. They clearly show variations in the continuum and in the He II $\lambda 4686$ line profile. Figure 2 shows the mean and the root mean square (rms) spectra of 3C 120 for our variability campaign. The rms spectrum is given at the bottom. This spectrum was scaled by a factor of ten (the zero level is shifted by -2.5) to enhance weaker line structures. The rms spectrum presents the variable part of the line profiles. Below we discuss the spectra in the context of the line profiles in 3C 120

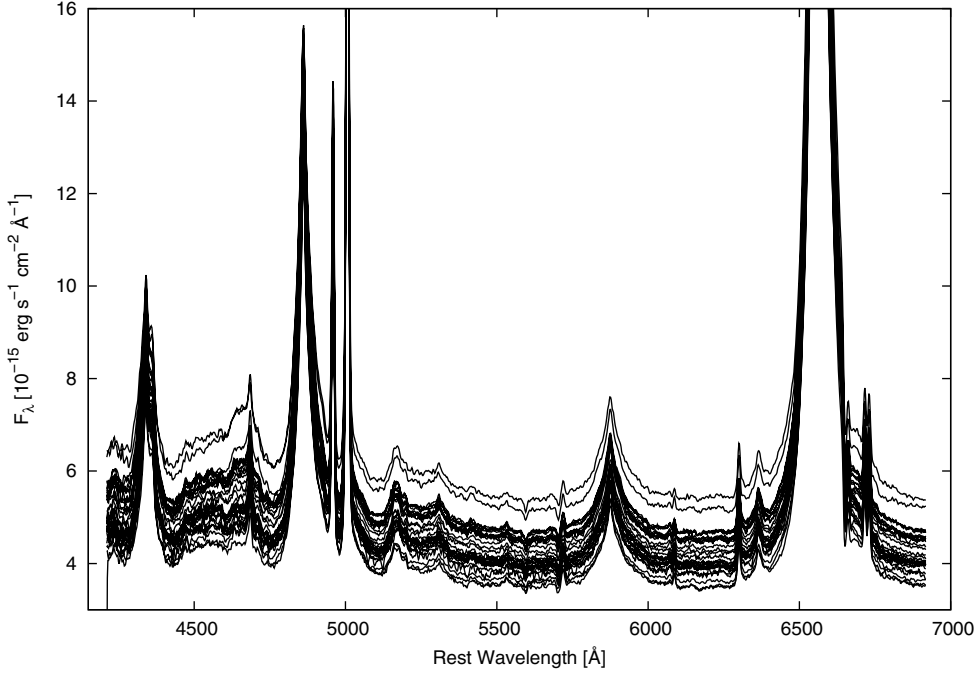


Fig. 1. Optical spectra of 3C 120 taken with the HET telescope.

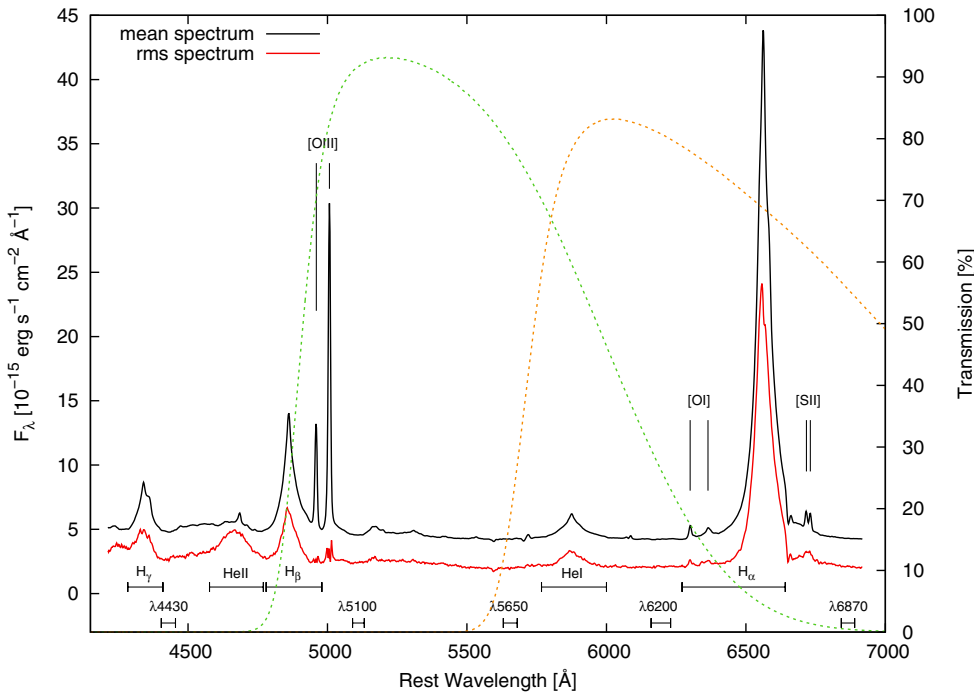


Fig. 2. Integrated mean (black) and rms (red) spectra of 3C 120. The rms spectrum has been scaled by a factor of 10 (the zero level is shifted by -2.5) to enhance weaker line structures. Overplotted are V (green) and R (orange) band filter curves. We also used these filters to generate the continuum light-curves.

Table 3. Rest frame continuum boundaries and line integration limits.

Cont./line (1)	Wavelength range (2)	Pseudo-continuum (3)
Cont. 4430	4424 Å–4440 Å	
Cont. 5100	5090 Å–5132 Å	
Cont. 5650	5630 Å–5680 Å	
Cont. 6200	6160 Å–6230 Å	
Cont. 6870	6842 Å–6890 Å	
H α	6271 Å–6641 Å	6160 Å–6890 Å
H β	4780 Å–4980 Å	4424 Å–5132 Å
H γ	4284 Å–4410 Å	4424 Å–5132 Å
He II λ 4686	4577 Å–4770 Å	4424 Å–5132 Å
He I λ 5876	5767 Å–6000 Å	5630 Å–6230 Å

in more detail. The continuum boundaries and line integration limits we used for the present study are given at the bottom of the spectra in Fig. 2. We selected the continuum boundaries in the following way: we inspected our mean and rms spectra for continuum regions that were free of both strong emission and absorption lines. The final wavelength ranges we used for the continuum flux measurements are given in Table 3. The continuum region at 5100 Å is often used for studies of the variable continuum flux in AGN. In general, this region is free of strong emission lines and close to the [O III] λ 5007 flux calibration line. In addition to this wavelength range at 5100 Å we determined the continuum intensities at four additional continuum ranges (at 4430, 5650, 6200, and 6870 Å, see Fig. 2 and Table 3). We used these continua to create pseudo-continua below the variable broad emission lines as well.

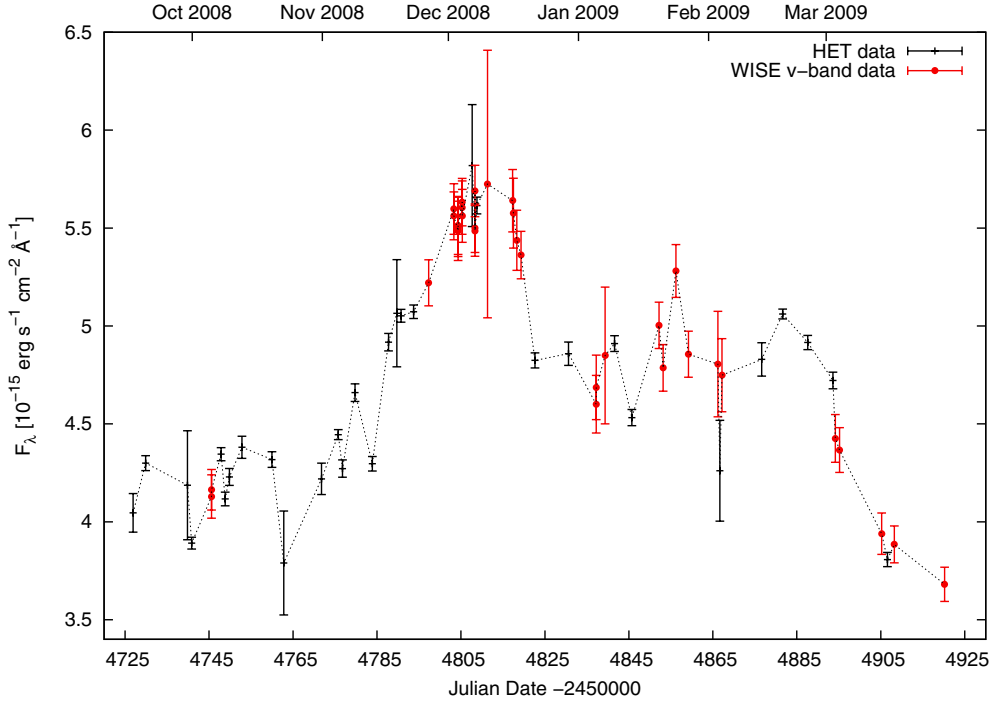


Fig. 3. Continuum light-curve at 5100 Å (including *V*-band data) for 3C 120.

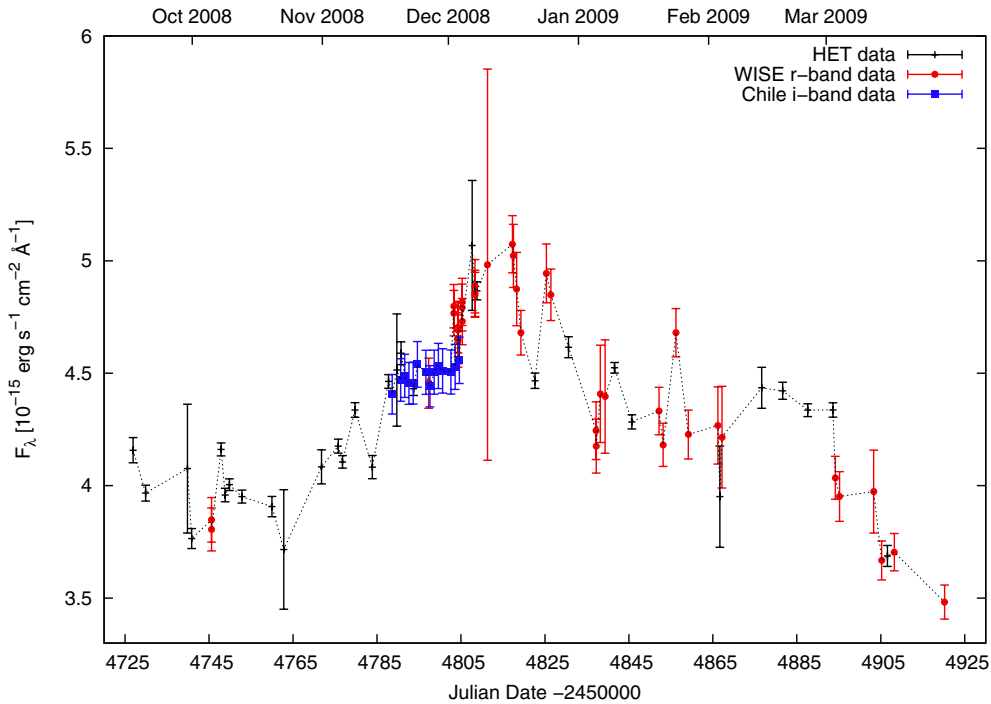


Fig. 4. Continuum light-curve at 6200 Å (including *R*-band, and intercalibrated *I*-band data) for 3C 120.

We integrated the broad emission-line intensities of the Balmer and helium lines between the wavelength boundaries given in Table 3. Figure 2 shows the selected wavelength ranges for the Balmer and helium lines. First we subtracted a linear pseudo-continuum defined by the boundaries given in Table 3 (Col. 3), then we integrated the emission-line flux. For H γ we extrapolated the continuum of the H β and He II λ 4686 measurements. The results of the continuum and line intensity measurements are given in Table 4.

3.2. Continuum and emission-line light curves

We show in Figs. 3 and 4 the continuum light-curves of 3C 120 at 5100 Å and 6170 Å for our variability campaign.

First we created light curves based on the HET spectra alone. Then we generated light curves based on the *V*- and *R*-band photometric data taken at Wise observatory. We intercalibrated the *V*-band photometry into the continuum light curve at 5100 Å and the *R*-band photometry into the continuum light curve at 6170 Å. We applied a multiplicative scale factor and an additional flux adjustment component to set the light curves on the same scale and to correct for differences in the host galaxy contribution. Finally, we also fitted the *I'*-band photometry observed at Cerro Armazones into the continuum light curve at 6170 Å. Overall, the light curves from different telescopes agree well. The individual continuum fluxes for the different epochs at 5100 Å and 6170 Å are given in Table 5. The light curve in the *V* band has a higher variation amplitude than the light curve in the *R* band,

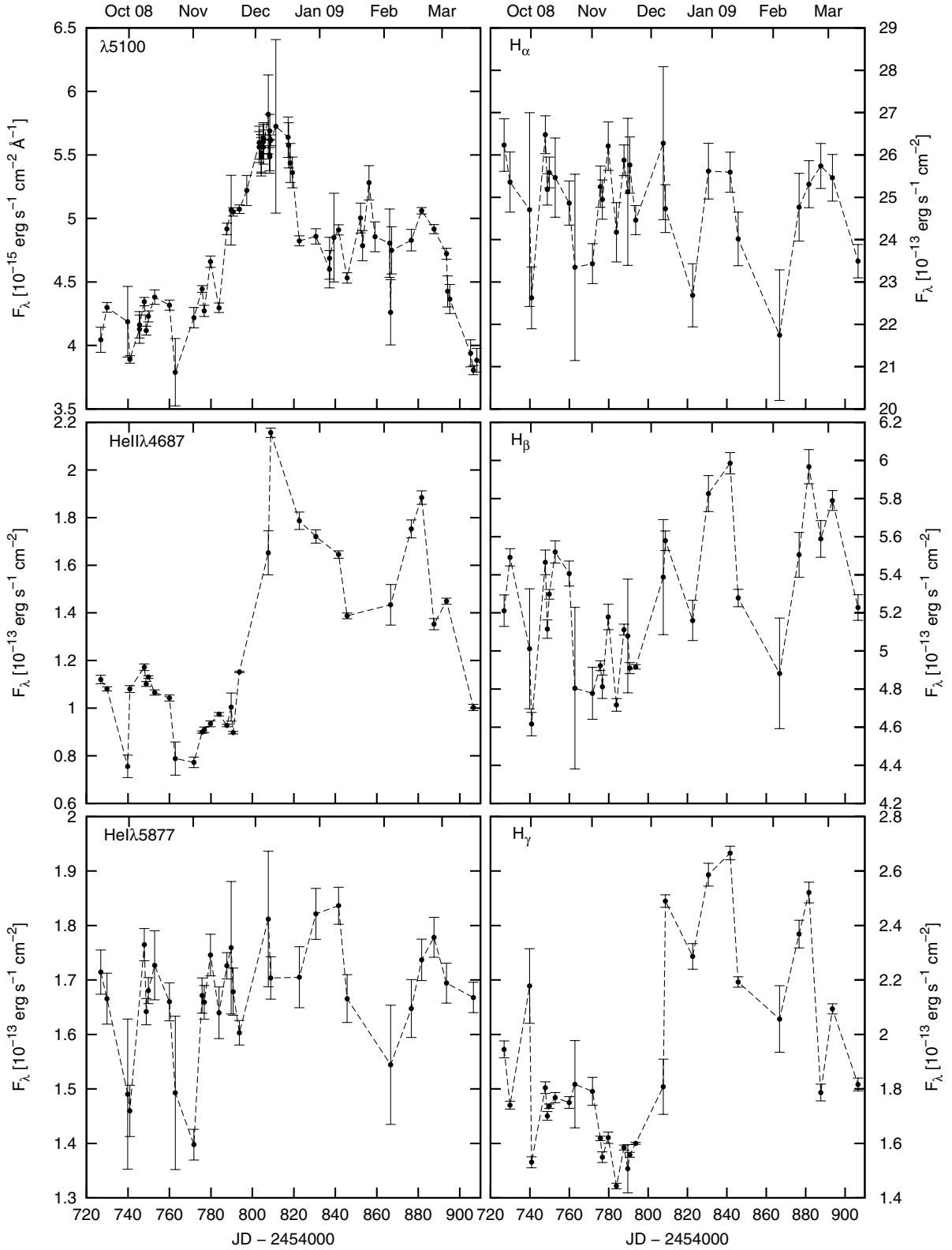


Fig. 5. Light curves of the continuum flux at 5100 \AA (in units of $10^{-15} \text{ erg cm}^{-2} \text{ s}^{-1} \text{ \AA}^{-1}$) and of the integrated emission-line fluxes of $\text{H}\alpha$, $\text{H}\beta$, $\text{H}\gamma$, $\text{He I } \lambda 4686$, and $\text{He I } \lambda 5876$ (in units of $10^{-13} \text{ erg cm}^{-2} \text{ s}^{-1}$).

as expected for AGN where the contribution of the nonthermal continuum flux is stronger in the blue.

In Fig. 5 we present the light curves of the integrated emission-line fluxes of the Balmer lines $\text{H}\alpha$, $\text{H}\beta$, and $\text{H}\gamma$, and of the helium lines $\text{He I } \lambda 5876$, $\text{He II } \lambda 4686$. The continuum light curve at 5100 \AA is shown for comparison. The line and

continuum flux values are given in Table 4. The mean continuum flux $F_{\lambda}(5100 \text{ \AA})$ is $4.57 \pm 0.23 \times 10^{-15} \text{ erg s}^{-1} \text{ cm}^{-2} \text{ \AA}^{-1}$ and the mean $\text{H}\beta$ flux $F(\text{H}\beta)$ is $5.24 \pm 0.39 \times 10^{-13} \text{ erg s}^{-1} \text{ cm}^{-2}$.

Some statistics of the continuum and emission line intensity variations is given in Table 6. We indicate the lowest and highest fluxes F_{\min} and F_{\max} , peak-to-peak amplitudes

Table 6. Variability statistics for 3C 120 in units of 10^{-15} erg s $^{-1}$ cm $^{-2}$ Å $^{-1}$ for the continuum (Cols. 2, 3, 5) and in units of 10^{-15} erg s $^{-1}$ cm $^{-2}$ for the emission lines (Cols. 2, 3, 5).

Cont./line (1)	F_{\min} (2)	F_{\max} (3)	R_{\max} (4)	$\langle F \rangle$ (5)	σ_F (6)	F_{var} (7)
Cont. 5100	3.79	5.82	1.54	4.57	0.491	0.104
Cont. 6200	3.69	5.07	1.37	4.24	0.32	0.071
H α	2174.5	2647.7	1.22	2485.6	117.07	0.028
H β	461.6	598.5	1.30	524.3	36.94	0.065
H γ	144.4	266.6	1.85	190.1	34.94	0.181
He I λ 5876	139.8	183.6	1.31	167.1	10.42	0.050
He II λ 4686	75.6	215.6	2.85	122.7	36.71	0.298

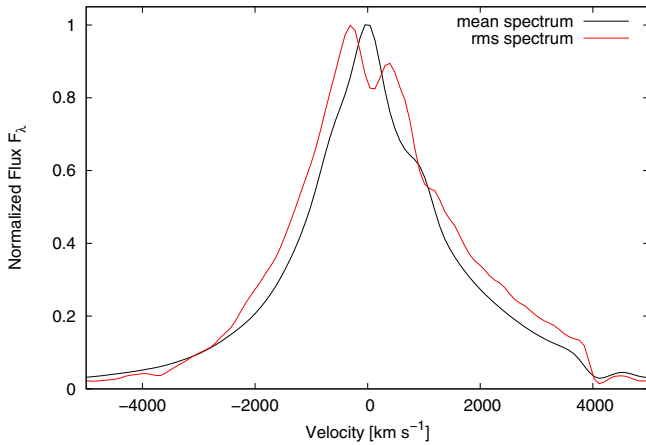


Fig. 6. Normalized mean (black) and rms (red) line profiles of H α in velocity space.

$R_{\max} = F_{\max}/F_{\min}$, the mean flux during the period of observations $\langle F \rangle$, the standard deviation σ_F , and the fractional variation

$$F_{\text{var}} = \frac{\sqrt{\sigma_F^2 - \Delta^2}}{\langle F \rangle}$$

as defined by Rodríguez-Pascual et al. (1997). The quantity Δ^2 is the mean square value of the uncertainties Δ_i associated with the fluxes F_i .

3.3. Mean and rms line profiles

Based on the observed spectra, we calculated normalized mean and rms line profiles of the Balmer lines H α , H β , H γ , and of the helium lines He I λ 5876, and He II λ 4686 after subtracting the continuum flux. They are presented in Figs. 6 to 12 in velocity space. We show in Figs. 6 to 10 the normalized mean and rms line profiles of the individual lines. The rms spectra illustrate the variations in the line profile segments during our variability campaign. The strong blue wing of the H γ rms line in Fig. 8 (i.e. short-wards of -2000 km s $^{-1}$) is probably caused by the strong blue variability of the underlying continuum (see Fig. 2). Because there is no continuum window on the blue side of the H γ line in our 3C 120 spectra we were unable to subtract a pseudo-continuum below the line with the same precision as for the other lines. In Figs. 11 and 12 we present all normalized mean profiles of the Balmer and helium lines and all normalized rms profiles. Thus we can compare the different line widths FWHM and different profile shapes and line asymmetries.

We present in Table 7 the line widths FWHM of the mean and rms line profiles of the Balmer and helium lines.

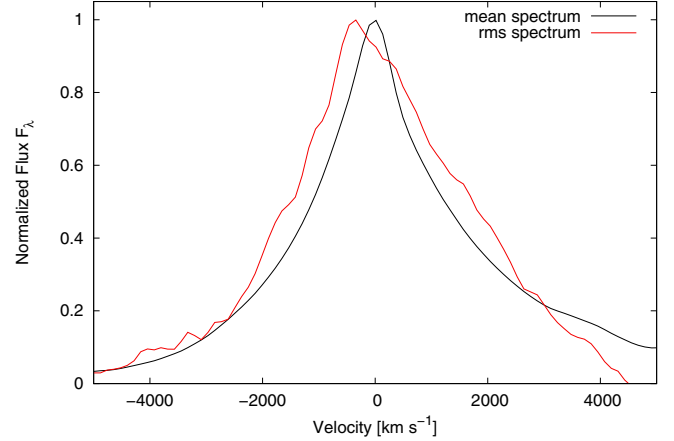


Fig. 7. Normalized mean (black) and rms (red) line profiles of H β in velocity space.

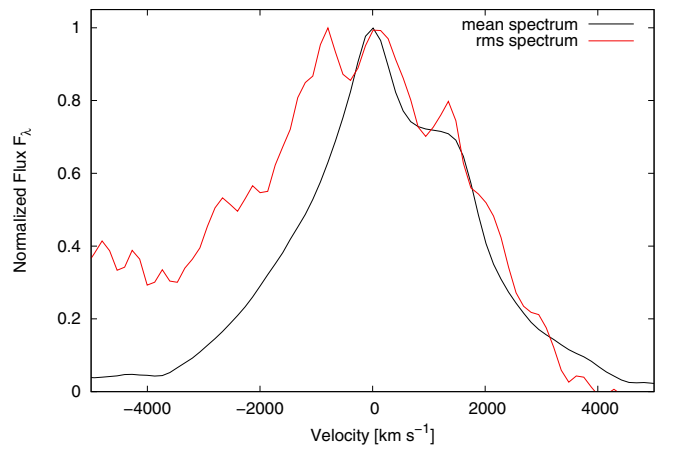


Fig. 8. Normalized mean (black) and rms (red) line profiles of H γ in velocity space. The strong blue wing in the rms profile is probably due to a poorly accounted continuum (as described in the text).

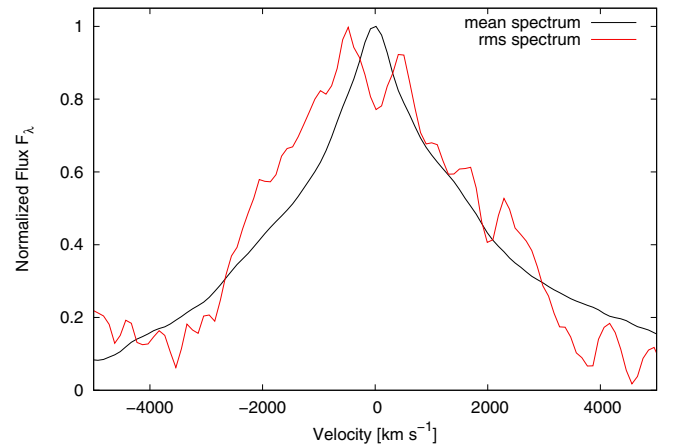


Fig. 9. Normalized mean (black) and rms (red) line profiles of He I λ 5876 in velocity space.

Furthermore, we parameterized the line widths of the rms profiles by their line dispersion σ_{line} (rms widths) (Fromerth & Melia 2000; Peterson et al. 2004). In Table 8 we display the shifts of the line centers of the rms and mean line profiles. We derived the emission line centers using only the parts of the line profiles above 75% of the peak value.

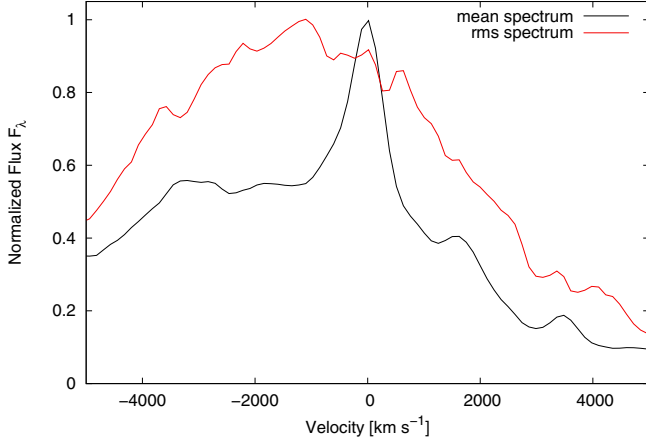


Fig. 10. Normalized mean (black) and rms (red) line profiles of He II $\lambda 4686$ in velocity space.

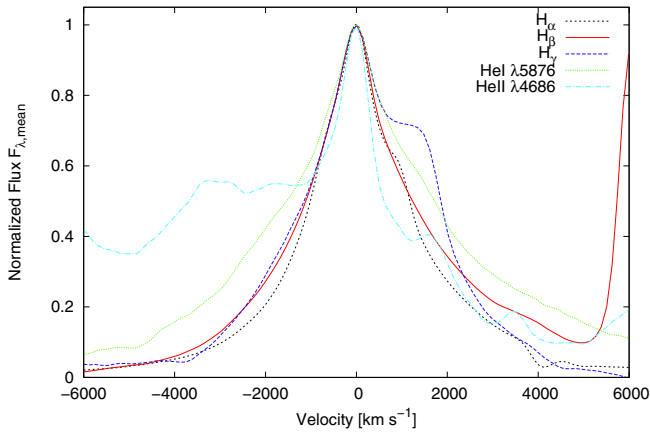


Fig. 11. Normalized mean line profiles of H α , H β , H γ , He I $\lambda 5876$, and He II $\lambda 4686$.

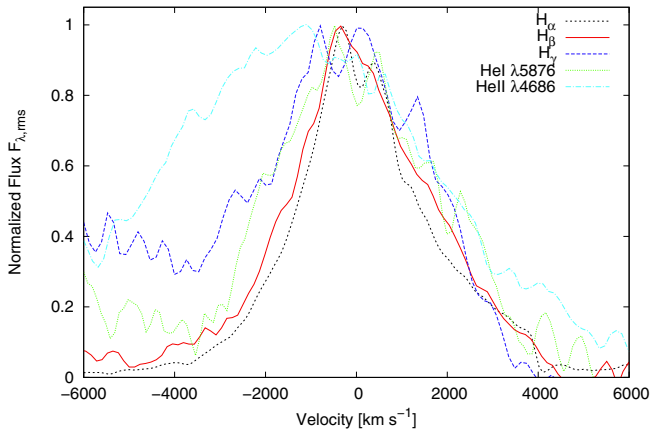


Fig. 12. Normalized rms line profiles of H α , H β , H γ , He I $\lambda 5876$, and He II $\lambda 4686$. The H γ wing blueward of 2000 km s $^{-1}$ is probably due to poor continuum modeling.

There are three clear trends in the mean and rms emission-line profiles in 3C 120:

- the individual rms profiles (FWHM) are always broader than the mean profiles;
- the (higher ionized) helium lines are always broader than the Balmer lines;
- the (higher ionized) helium rms profiles exhibit stronger blueshifts and asymmetries than the Balmer lines.

Table 7. Balmer and helium line widths: FWHM of the mean and rms line profiles and line dispersion σ_{line} (rms width) of the rms profiles.

Line	FWHM (mean) [km s $^{-1}$]	FWHM (rms) [km s $^{-1}$]	σ_{line} (rms) [km s $^{-1}$]
(1)	(2)	(3)	(4)
H α	2205 \pm 74	2630 \pm 87	1638 \pm 105
H β	2386 \pm 52	3252 \pm 67	1689 \pm 68
H γ	3029 \pm 65	4696 \pm 979	1939 \pm 78
He I $\lambda 5876$	2962 \pm 99	3987 \pm 128	2358 \pm 570
He II $\lambda 4686$	5821 \pm 1297	6472 \pm 132	3253 \pm 130

Table 8. Line center (above 75% of the peak value) in the rms and mean line profiles.

Line center	rms profile [km s $^{-1}$]	Mean profile [km s $^{-1}$]
(1)	(2)	(3)
H α	-145.5 \pm 137.	-19.0 \pm 18.5
H β	-191.6 \pm 104.	-16.7 \pm 25.1
H γ	-199.8 \pm 57.	+33.3 \pm 28.2
He I $\lambda 5876$	-213.4 \pm 171.	+11.4 \pm 19.2
He II $\lambda 4686$	-1197.4 \pm 66.	-29.7 \pm 25.8

These trends indicate that the variable part of the emission-line profiles (i.e., the rms spectrum) originates closer to the center – where the rotation velocity is higher – than the non-variable part. Furthermore, the (higher ionized) helium lines also originate closer to the center than the Balmer lines. A blueshift in the rms profiles in comparison with symmetric mean profiles can be explained by an additional outflow component that is moving towards the observer. In disk-wind models the more distant receding part of the wind is occulted by the accretion disk so that the red side of the line profile of a high-ionization line is suppressed (e.g. Gaskell 2009).

3.4. CCF analysis

The distance of the broad-line emitting region from the central ionizing source can be estimated in AGN by correlating the broad emission-line light curves with that of the ionizing continuum flux. A continuum light curve in the optical is normally used as surrogate for the ionizing light curve. An interpolation cross-correlation function method (ICCF) has been developed by Gaskell & Peterson (1987) to calculate the delay of the two light curves. We developed our own ICCF code (Dietrich & Kollatschny 1995) in a similar way. With this method we correlated the light curves of the Balmer and helium lines of 3C 120 with the continuum light curve at 5100 Å. The cross-correlation functions ICCF(τ) are presented in Fig. 13. We derived the centroids of these ICCF, τ_{cent} , by using only the part of the CCF above 80% of the peak value. It has been shown by Peterson et al. (2004) that a threshold value of 0.8 r_{max} is generally a good choice. We determined the uncertainties in our cross-correlation results by calculating the cross-correlation lags many times using a model-independent Monte Carlo method known as *flux redistribution/random subset selection* (FR/RSS). This method has been described by Peterson et al. (1998). Here the error intervals correspond to 68% confidence levels.

The final results of the ICCF analysis are given in Table 9. The delay of the integrated H β line with respect to the continuum light curve at 5100 Å corresponds to 28.5 $^{+9.0}_{-8.5}$ light-days. The

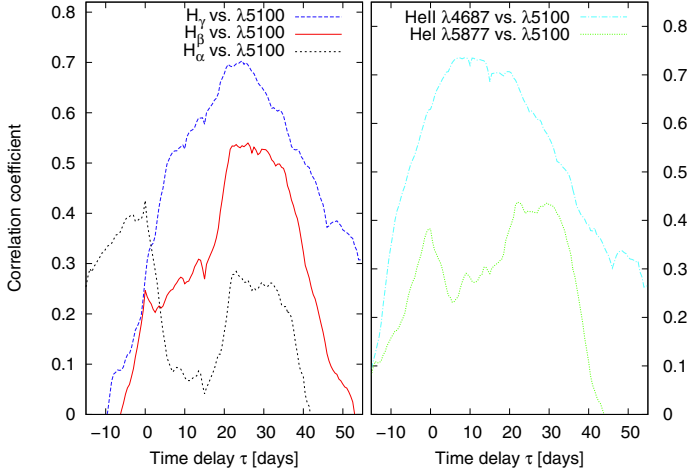


Fig. 13. Cross-correlation functions $CCF(\tau)$ of the Balmer and helium line light curves compared with the continuum light curve at 5100 \AA .

Table 9. Cross-correlation lags of the Balmer and helium line light curves with respect to the 5100 \AA continuum light curve.

Line (1)	τ [days] (2)
H α	$28.5^{+9.0}_{-8.5}$
H β	$27.9^{+7.1}_{-5.9}$
H γ	$23.9^{+4.6}_{-3.9}$
He I $\lambda 5876$	$26.8^{+6.7}_{-7.3}$
He II $\lambda 4686$	$12.0^{+7.5}_{-7.0}$

other Balmer lines and the He I $\lambda 5876$ show similar delays of 24 to 28 light-days. The delay of the integrated He II $\lambda 4686$ line only corresponds to $12.0^{+7.5}_{-7.0}$ light-days. It is known that there is a radial BLR stratification in AGN (e.g. Kollatschny 2003). The higher ionized lines show broader line widths (FWHM) and originate closer to the center (Fig. 14). In a similar way, the variability amplitude of the integrated emission lines is correlated with the distance of the line-emitting region to the central ionizing source (Fig. 15). We present in Fig. 14 the theoretical relation between distance and line width for different black hole masses based on the mass formula given in Sect. 3.5. For this diagram we used the corrected rotational velocities v_{rot} given in Table 10. It shows the known trend that the He II $\lambda 4686$ line originates closer to the center than the Balmer lines and the He I $\lambda 5876$ line.

3.5. Central black hole mass

The central black hole mass in AGN can be derived from the width of the broad emission-line profiles based on the assumption that the gas dynamics are dominated by the central massive object, by evaluating $M = f c \tau_{\text{cent}} \Delta v^2 G^{-1}$. The characteristic distance of the line-emitting region τ_{cent} is given by the centroid of the individual cross-correlation functions of the emission-line variations compared with the continuum variations (e.g. Koratkar & Gaskell 1991; Kollatschny & Dietrich 1997). The characteristic velocity Δv of the emission-line region can be estimated from the FWHM of the rms profile or from the line dispersion σ_{line} .

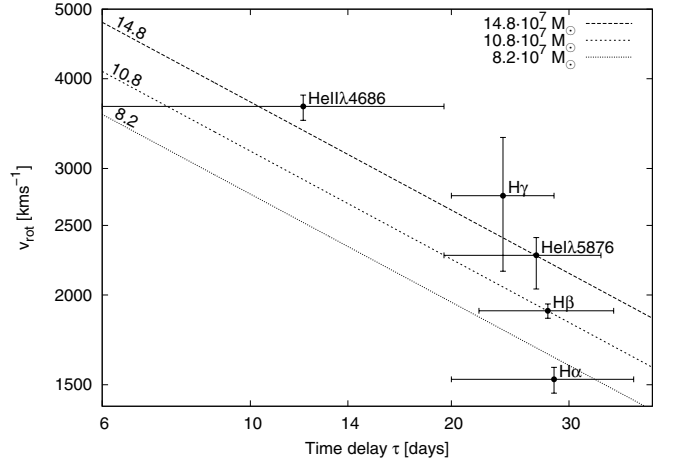


Fig. 14. Line width of the emission lines (given by v_{rot}) as function of their time delay τ (i.e. distance to the center). The dotted and dashed lines correspond to virial masses of 14.8 , 10.8 , and $8.2 \times 10^7 M_{\odot}$.

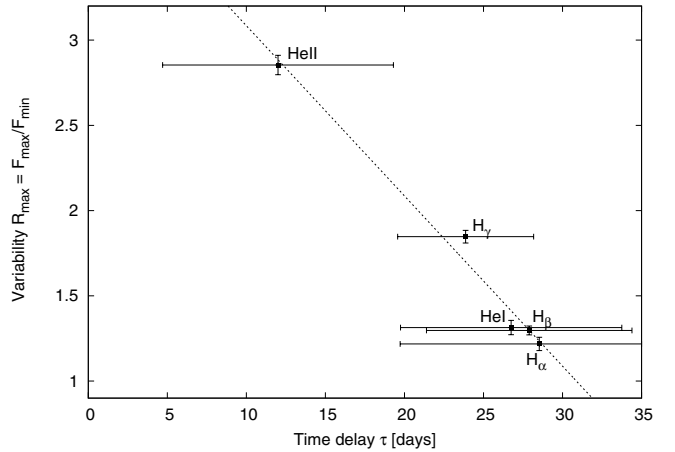


Fig. 15. Variability amplitude of the integrated emission lines as function of their time delay τ (i.e. distance to the center). The dotted line is the best fit to the data.

The scaling factor f in the equation above is on the order of unity and depends on the kinematics, structure, and orientation of the BLR. This scaling factor may differ from galaxy to galaxy depending on whether we see the central accretion disk including the BLR from the edge or face-on. We wish to compare our value of the central black hole mass in 3C 120 with values of the black hole mass derived by other authors (i.e., Grier et al. 2012) and therefore, we adopted their mean value of $f = 5.5$.

Based on the derived delay of the integrated H β line ($\tau_{\text{cent}} = 27.9 \pm 6.5$ days) and on the H β line width ($FWHM(\text{rms}) = 3252 \pm 67 \text{ km s}^{-1}$), we calculate a black hole mass of

$$M = 3.1 \pm 0.7 \times 10^8 M_{\odot}.$$

However, here we did not correct for the contribution of turbulent motions to the width of the line profiles so far. This is presented in Sect. 3.7 in more detail. After correcting the H β line width (FWHM) for its contribution of turbulent motions we derived a black hole mass of

$$M = 10.8 \pm 2.6 \times 10^7 M_{\odot}.$$

Grier et al. (2012) derived a black hole mass of $M = 6.7 \pm 0.6 \times 10^7 M_{\odot}$ based on the line dispersion σ_{line} of her H β data. The two values agree well.

Table 10. Line profile parameters and radius and height of the line-emitting regions for individual emission lines in 3C 120.

Line	$FWHM/\sigma$	v_{turb} [km s ⁻¹]	v_{rot} [km s ⁻¹]	Radius [ld]	Height [ld]	H/R	Height _{corr} [ld]	H_{corr}/R	log10(λL_{λ}) [erg s ⁻¹]
He II $\lambda 4686$	1.99 ± 0.09	1993^{+347}_{-319}	3661^{+135}_{-160}	$12.0^{+7.5}_{-7.0}$	6.5 ± 4.2	0.54	3.0 ± 2.2	0.25	44.12 ± 0.07
H γ	2.42 ± 0.16	486^{+132}_{-128}	2750^{+564}_{-592}	$23.9^{+4.6}_{-3.9}$	4.2 ± 1.4	0.18	3.7 ± 1.4	0.15	.
He I $\lambda 5876$	1.69 ± 0.27	1139^{+609}_{-483}	2271^{+133}_{-232}	$26.8^{+6.7}_{-7.3}$	13.4 ± 8.2	0.50	9.4 ± 7.7	0.35	.
H β	1.93 ± 0.09	507^{+73}_{-70}	1901^{+42}_{-45}	$27.9^{+7.1}_{-5.9}$	7.4 ± 2.2	0.27	5.9 ± 1.8	0.21	.
H α	1.61 ± 0.12	548^{+108}_{-101}	1526^{+60}_{-66}	$28.5^{+9.0}_{-8.5}$	10.2 ± 3.8	0.36	13.1 ± 4.6	0.46	.
H β (p04)	1.89 ± 0.18	243^{+48}_{-49}	1291^{+109}_{-110}	$38.1^{+21.3}_{-15.3}$	7.2 ± 4.3	0.19	11.8 ± 6.8	0.31	44.01 ± 0.05
H β (g12)	1.68 ± 0.32	453^{+106}_{-110}	1480^{+280}_{-294}	$25.6^{+2.4}_{-2.4}$	7.8 ± 2.6	0.30	6.9 ± 2.4	0.27	43.87 ± 0.05

Notes. The H β parameters and the continuum luminosities are given for three observing campaigns.

Based on the similarly corrected line widths (FWHM) of the additional Balmer and helium lines and on their derived delays, we calculated black hole masses of 7.7 ± 2.3 (H α), 19.4 ± 8.9 (H γ), 14.8 ± 4.6 (He I $\lambda 5876$), and $17.3 \pm 10.5 \times 10^7 M_{\odot}$ (He II $\lambda 4686$). All these BH masses agree with each other within the error limits.

3.6. 2D CCF of the Balmer (H α , H β , H γ) and helium I, II line profiles

In this section we investigate in more detail the profile variations of the Balmer and helium lines in 3C 120. We proceed in the same way as for the line profile variations in Mrk 110 (Kollatschny & Bischoff 2002; Kollatschny 2003) and Mrk 926 (Kollatschny & Zetzl 2010).

We sliced the velocity profiles of the Balmer and helium lines into velocity segments of widths $\Delta v = 400 \text{ km s}^{-1}$. This value of 400 km s^{-1} corresponds to the spectral resolution of our observations. Then we measured the intensities of all subsequent velocity segments from $v = -3800$ until $+3800 \text{ km s}^{-1}$ and compiled their light curves. The central line segment was integrated from $v = -200$ until $+200 \text{ km s}^{-1}$. Light curves of the central H β segment, and of selected blue and red segments are shown in Fig. 16. For comparison, the light curve of the continuum flux at 5100 \AA is given as well.

We computed CCFs of all line segment ($\Delta v = 400 \text{ km s}^{-1}$) light curves of the Balmer and helium lines with the 5100 \AA continuum light curve. The derived delays of the segments compared with the 5100 \AA continuum light curve are shown in Figs. 17 to 21 as a function of distance to the line center. These 2D CCFs are presented in gray scale. The white lines in Figs. 17–21 delineate the contour lines of the correlation coefficient at different levels. The black curves show computed escape velocities for central masses of $3.5, 7, 14 \times 10^7 M_{\odot}$ (from bottom to top, see, e.g., Kollatschny & Bischoff 2002).

The light curves of the line centers are mostly delayed by 20 to 35 days with respect to the continuum variations – except for He II $\lambda 4686$. The outer line wings at distances of 2000 to 3000 km s^{-1} respond much faster to continuum variations than the inner line profile segments, by 0 to only 20 days. The outer blue wing of the H β line (shortward of -3000 km s^{-1}) is blended with the red wing of the He II $\lambda 4686$ line (see Fig. 2). Therefore the response shortward of -3000 km s^{-1} is influenced by the He II $\lambda 4686$ line. In contrast to the Balmer and He I lines, the He II $\lambda 4686$ line originates at a distance of only about 11 light days (Fig. 21, Table 9). And there is no indication for a longer

delay of the line center with respect to the line wings. In the discussion section we compare our observed velocity delay maps in more detail with model calculations of echo images from the BLR and with other observations.

3.7. Vertical BLR structure in 3C 120

We demonstrated in recent papers (Kollatschny & Zetzl 2011, 2013a,b,c) that we are able to make statements about the BLR structure in AGN based on variability studies in combination with line profile studies. The broad emission-line profiles in AGN can be parameterized by the ratio of their FWHM to their line dispersion σ_{line} . There exists a general relation between the full-width at half maximum and the line-width ratio $FWHM/\sigma_{\text{line}}$ for the individual emission lines.

The line width FWHM reflects the line broadening due to rotational motions of the broad-line gas of the intrinsic Lorentzian profiles that are associated with turbulent motions. Different emission lines are connected with different turbulent velocities.

Here we model the observed line width ratios $FWHM/\sigma_{\text{line}}$ versus the line width FWHM of 3C 120 (Fig. 22, Table 10) in the same way as for other Seyfert galaxies (Kollatschny & Zetzl 2011, 2013a,b,c). Based on their observed line widths (FWHM) and line-width ratios $FWHM/\sigma_{\text{line}}$, we plot in Fig. 22 the locations of all observed emission lines in 3C 120. We derived the rotational velocities that belong to the individual lines from their positions between the vertical dashed lines that represent different v_{rot} . The given H β line width ratios in Fig. 22 are based on three different variability campaigns: the variability campaign presented in this paper and two additional variability campaigns carried out by Peterson et al. (2004) and Grier et al. (2012). They are marked with *p04* and *g12* in Figs. 22–26 and Table 10.

We determined the heights of the line-emitting regions above the midplane on the basis of the turbulent velocities that belong to the individual emission lines as for other Seyfert galaxies. We used the following mean turbulent velocities: 425 km s^{-1} for H γ , 400 km s^{-1} for H β , 700 km s^{-1} for H α , 900 km s^{-1} for He II $\lambda 4686$. In Table 10 we present the derived heights above the midplane of the line-emitting regions in 3C 120 (in units of light-days) and the ratio H/R for the individual emission lines. The ratio of the turbulent velocity v_{turb} compared with the rotational velocity v_{rot} in the line-emitting region gives us information on the ratio of the accretion disk height H with respect to the accretion disk radius R of the line-emitting regions as presented in

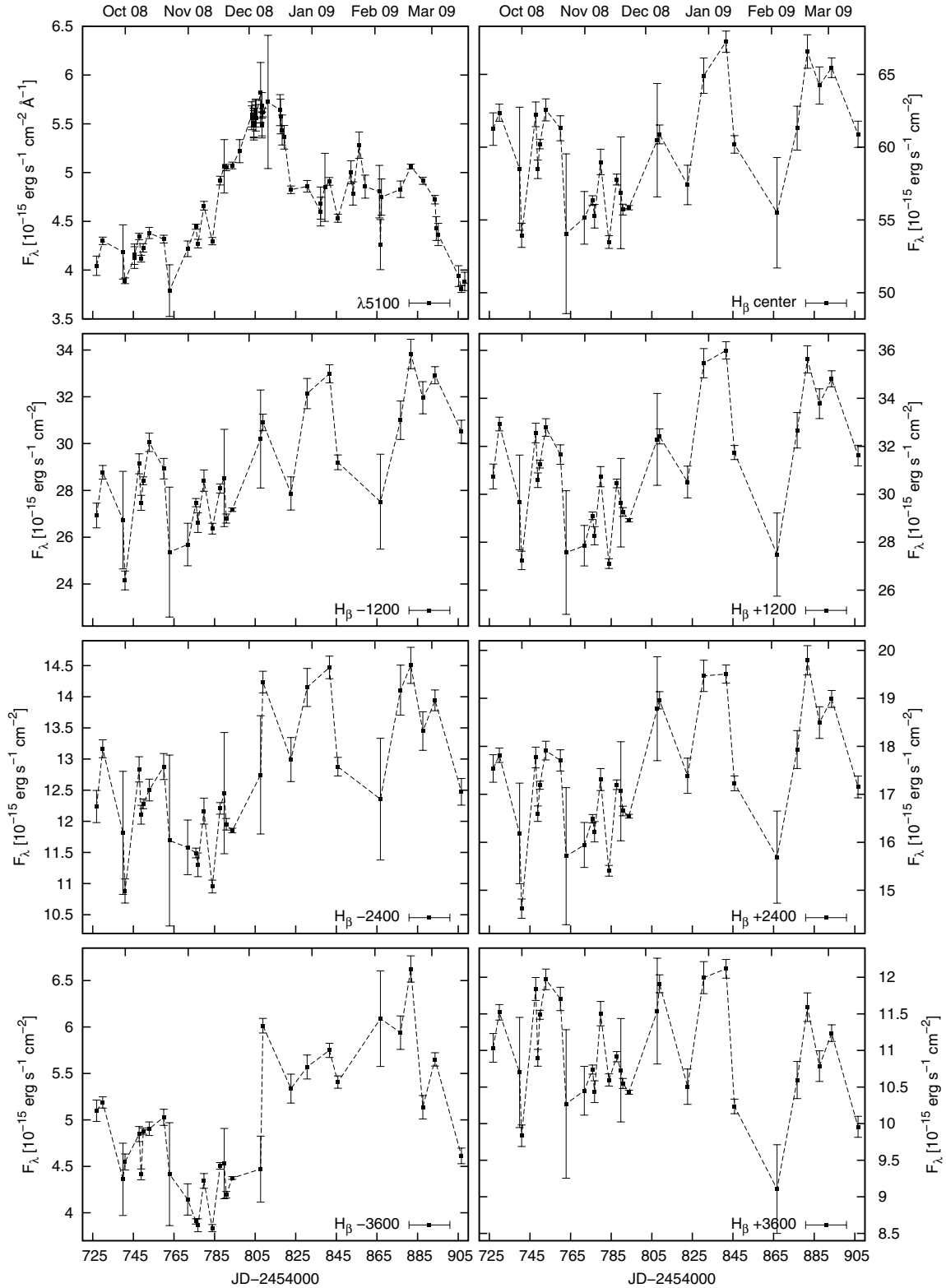


Fig. 16. Light curves of the continuum flux at 5100 Å and of selected H β line segments (in units of 10^{-15} erg s $^{-1}$ cm $^{-2}$): H β _{center}, and segments at $v = \pm 1200, \pm 2400, \pm 3600$ km s $^{-1}$.

Kollatschny & Zetzl (2011, 2013a):

$$H/R = (1/\alpha)(v_{\text{turb}}/v_{\text{rot}}). \quad (1)$$

The unknown viscosity parameter α is assumed to be constant and to have a value of one. We have not yet derived the mean turbulent velocity connected to the He I $\lambda 5876$ emission-line

region in AGN in our earlier papers. Based on Fig. 22, we computed a value on the order of 800 km s $^{-1}$ for He I $\lambda 5876$ from this single variability campaign.

We show in Fig. 23 the BLR structure of 3C 120 as a function of distance to the center and height above the midplane. The H β emission regions observed at different epochs are connected

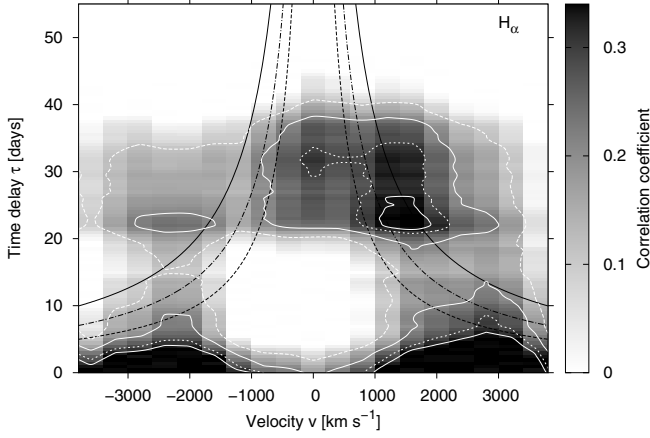


Fig. 17. 2D CCF(τ, v) showing the correlation of the $H\alpha$ line segment light curves with the continuum light curve as a function of velocity and time delay (gray scale). Contours of the correlation coefficients are overplotted at levels of 0.32, 0.28, 0.2, 0.1 (white lines). The black curves show computed escape velocities for central masses of $3.5, 7, 14 \times 10^7 M_{\odot}$ (from bottom to top).

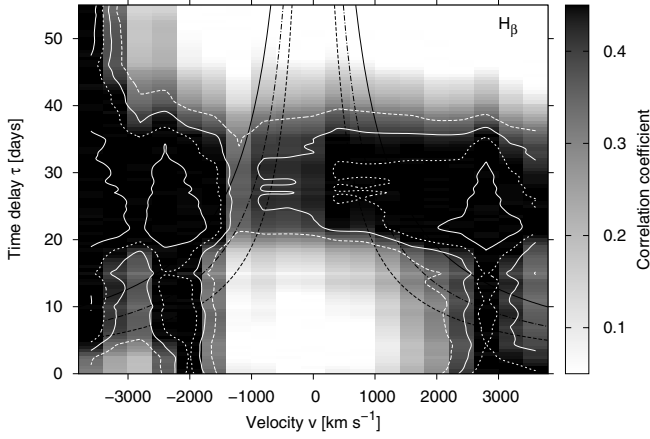


Fig. 18. 2D CCF(τ, v) showing the correlation of the $H\beta$ line segment light curves with the continuum light curve as a function of velocity and time delay (gray scale). Contours of the correlation coefficients are overplotted at levels of 0.53, 0.46, 0.4, 0.32 (white lines). Black curves as in Fig. 17.

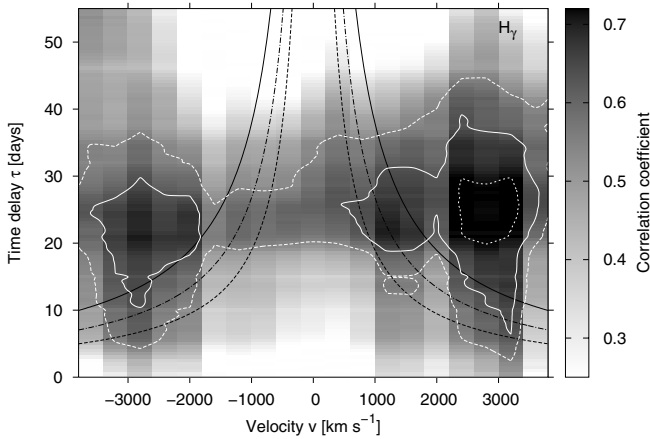


Fig. 19. 2D CCF(τ, v) showing the correlation of the $H\gamma$ line segment light curves with the continuum light curve as a function of velocity and time delay (gray scale). Contours of the correlation coefficients are overplotted at levels of 0.71, 0.62, 0.53 (white lines). Black curves as in Fig. 17.

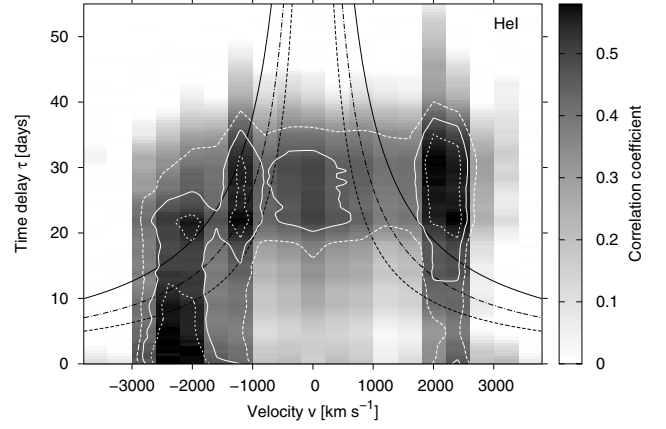


Fig. 20. 2D CCF(τ, v) showing the correlation of the $He I \lambda 5876$ line segment light curves with the continuum light curve as a function of velocity and time delay (gray scale). Contours of the correlation coefficients are overplotted at levels of 0.52, 0.44, 0.34 (white lines). Black curves as in Fig. 17.

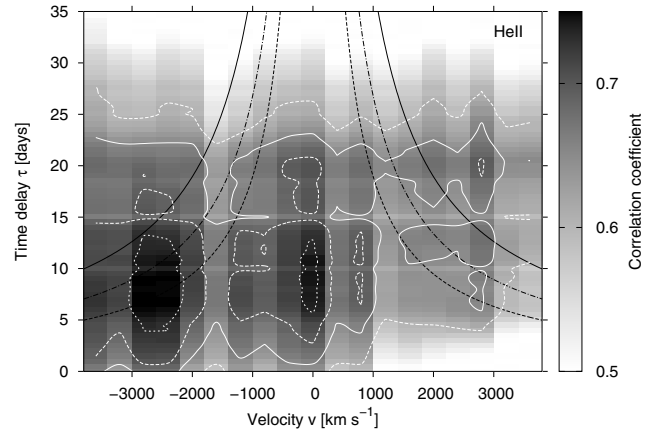


Fig. 21. 2D CCF(τ, v) showing the correlation of the $He II \lambda 4686$ line segment light curves with the continuum light curve as a function of velocity and time delay (gray scale). Contours of the correlation coefficients are overplotted at levels of 0.72, 0.68, 0.64, 0.59 (white lines). Black curves as in Fig. 17.

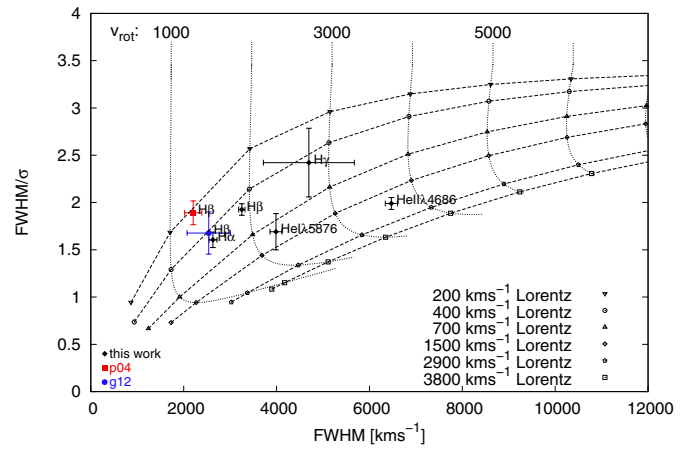


Fig. 22. Observed and modeled line-width ratios $FWHM/\sigma_{\text{line}}$ versus line width $FWHM$ in 3C 120. The dashed curves represent the corresponding theoretical line-width ratios based on rotational line-broadened Lorentzian profiles ($FWHM = 200$ to 3800 km s^{-1}). The rotation velocities reach from 1000 to 6000 km s^{-1} (curved dotted lines from left to right).

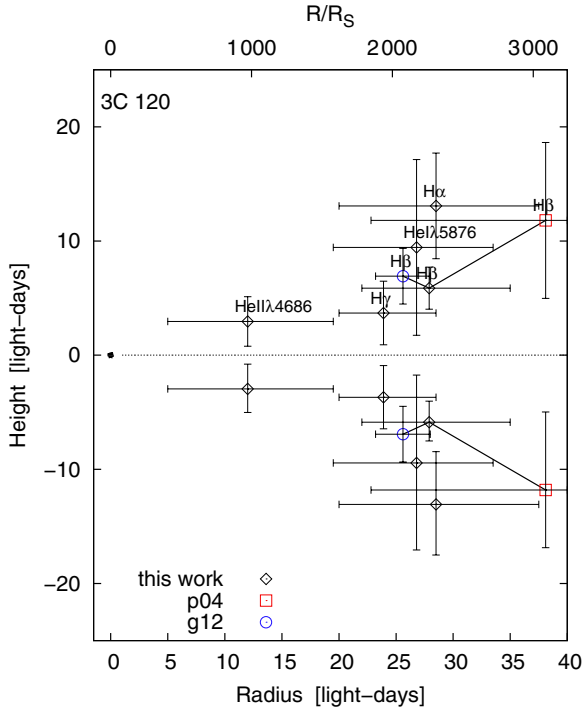


Fig. 23. Structure of the BLR in 3C 120. The $H\beta$ positions for the three variability campaigns are connected by a solid line. The dot at radius zero has the size of a Schwarzschild black hole (for $M_{\text{BH}} = 10.8 \times 10^7 M_{\odot}$) multiplied by a factor of twenty.

by a solid line. The errors are large for the $H\beta$ region of the variability campaign of the years 1989–1996 (Peterson et al. 1998) because of poor sampling. The dot at radius zero gives the size of the Schwarzschild radius $R_S = 1.2 \times 10^{-2} \text{ ld} = 3.2 \times 10^{13} \text{ cm}$ for a black hole mass (with $M = 10.8 \times 10^7 M_{\odot}$) multiplied by a factor of twenty. The label at the top of the figure gives the distances of the line-emitting regions in units of the Schwarzschild radius. The $\text{He II } \lambda 4686$ line originates at the shortest distance from the center and smallest height above the midplane in comparison with the Balmer and He I lines, as has been seen before in other galaxies. $H\alpha$ originates at a larger distance from the midplane than $H\beta$. This has also been seen before in NGC 7469 (Kollatschny & Zetzl 2013c). Here we see the same effect in 3C 120.

4. Discussion

We monitored 3C 120 in the years 2008 and 2009. At this time the AGN was in a brighter state (Fig. 3) than in observations taken earlier during the years 1989–1996 (Peterson et al. 1998) or later during the year 2010 (Grier et al. 2012) (see the mean continuum luminosities given in Table 10). In our discussion section we highlight the line-profile variations in 3C 120 during our campaign in comparison with other variability campaigns. Furthermore, we discuss the results regarding the BLR structure in 3C 120 in comparison with the BLR structure in other AGN.

4.1. Structure and kinematics in the BLR of 3C 120

The response of emission-line segments compared with the variable ionizing continuum does not only give information about the distance of the line-emitting regions, but also on their kinematics in comparison with model calculations. These 2D

CCF(τ, v) are mathematically very similar to 2D response functions Ψ (Welsh 2001).

Our 2D cross-correlation functions CCF(τ, v) of the Balmer ($H\alpha$, $H\beta$, $H\gamma$) and helium ($\text{He I } \lambda 5876$, $\text{He II } \lambda 4686$) line segment light curves with the continuum light curve at 5100 \AA are presented in Figs. 17 to 21 as a function of velocity and time delay (gray scale). There is a general trend to be seen in the Balmer and $\text{He I } \lambda 5876$ lines that the emission-line wings at distances of 2000 to 3000 km s^{-1} from the line center respond much faster than the central region. The centers of these lines respond with a delay of 25–30 light-days with respect to the ionizing continuum, while the response in the wings is much faster, with delays of 0–20 light-days.

Grier et al. (2013) monitored the variability in the $H\beta$, $H\gamma$, and $\text{He II } \lambda 4686$ lines of 3C 120 one and a half years later than we did. They also reported a lack of prompt response in the line centers of $H\beta$ and $H\gamma$ in 3C 120. The faster response in the Balmer line wings compared with that of to the line center has been seen in variability campaigns of other AGN as well, for example, in Mrk 110 (Kollatschny 2003), NGC 5548 (Kollatschny & Dietrich 1996 and Denney et al. 2009), SBS 1116 (Bentz et al. 2009), NGC 4593 (Kollatschny & Dietrich 1997). The faster response of the line wings is explained by accretion disk models for the line-emitting regions (e.g. Perez et al. 1992, or Welsh & Horne 1991). The BLR Keplerian disk model of Welsh & Horne (1991) (their Fig. 1c) agrees remarkably well with our Balmer and $\text{He I } \lambda 5876$ line observations.

Many of the Seyfert galaxies that have been monitored spectroscopically show indications for additional velocity components in the velocity-delay maps, that is, a stronger and faster response in the red or the blue wing. An earlier response in the blue line wing than in the red wing is connected with outflow motions in the models of Perez et al. (1992) and Horne et al. (2004). In disk-wind models the blue side of a line profile responds to changes in the ionizing continuum with almost no lag, while the red side of the line follows with twice the lag of the line as a whole (Gaskell 2009). An earlier response in the red wings is connected with inflow motions. On the other hand, an earlier response of the red line wing than in the blue line wing is predicted in the spherical wind and disk-wind models of Chiang & Murray (1996). In their models the line-emitting gas shows a radial outward velocity component in addition to the rotation.

Only a few galaxies present a shorter response in the blue $H\beta$ wings than in the red wings in the 2D cross-correlation functions as seen in Mrk 817 or NGC 3227 (Denney et al. 2010). On the other hand, most of the monitored Seyfert galaxies show a shorter and stronger response in their red Balmer wings than in the blue wings. Typical examples are Mrk 110 (Kollatschny 2003), Arp 151 (Bentz et al. 2010), Mrk 1501, and PG 2130 (Grier et al. 2013). Grier et al. (2013) found a stronger response in the red wings in both the $H\beta$ and $\text{He II } \lambda 4686$ emission-line profiles of 3C 120 as well. They explained their observing result by infall in addition to rotational motions in the BLR.

We monitored 3C 120 one and a half years earlier than Grier et al. (2013) at a time when this galaxy was in a bright state (see Table 10). The log of the mean continuum luminosity amounted to $\log_{10}(\lambda L_{\lambda}) = 44.12$ compared with 43.87 one and a half years later (Grier et al. 2013). The pattern of our $H\beta$ velocity delay map is similar to that of Grier et al. (2013), demonstrating a stronger response in the red wing. The pattern of the $H\alpha$ line we observed during our campaign shows a similar response as well. However, our $\text{He I } \lambda 5876$ and $\text{He II } \lambda 4686$ lines exhibit a stronger response in the blue wings than in the red wings. Furthermore, the blue wing in the $\text{He II } \lambda 4686$ line shows a shorter response

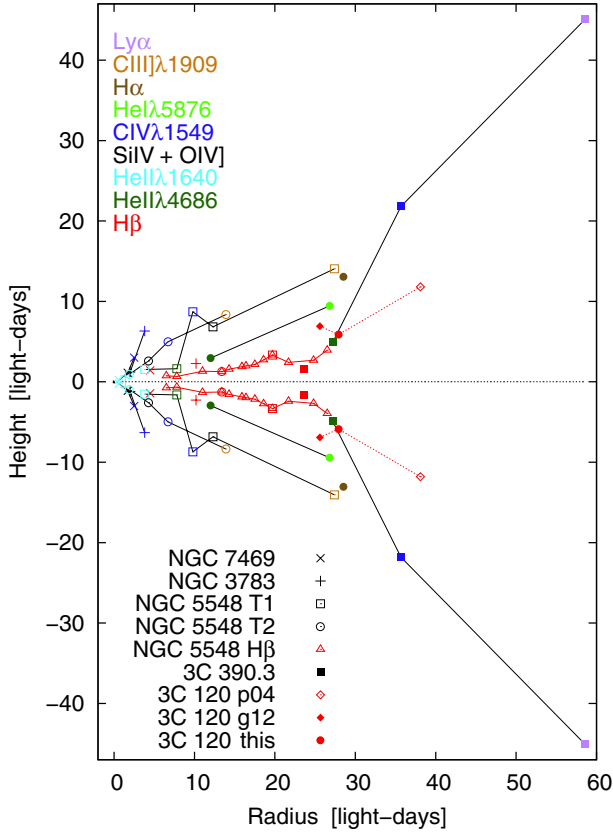


Fig. 24. BLR structures in 3C 120 (for three epochs), NGC 7469, NGC 3783, NGC 5548 (for two and 13 epochs), and 3C 390.3 as a function of distance to the center and height above the midplane (based on corrected turbulent velocities v_{turb}). The highly ionized (non-Balmer) lines of the individual galaxies are connected by a solid line. The $H\beta$ emitting regions are drawn in red. The three $H\beta$ line-emitting regions of 3C 120 are connected by a dot-dashed red line and those of NGC 5548 (13 epochs) are connected by a solid red line.

than the red wing. This is the opposite to what was observed by Grier et al. (2013) one and a half years later when the galaxy was in a lower state. A stronger and shorter response in the blue line wings is attributed to outflow motions in the models of Horne et al. (2004), for example. This points to outflow motions when the galaxy 3C 120 was in a higher activity state. This applies particularly to the He II $\lambda 4686$ line, which originates closer to the central ionizing source. Outflow motions are in accordance with the evidence for stronger variability in the blue line wings and the blue line asymmetries based on our rms profiles. Radial velocity offsets due to mass outflows in AGN have been discussed before, for instance by Crenshaw et al. (2010) and references therein.

There are indications in a few other galaxies that the response in the line wings varied with time, for example, the response in the C IV $\lambda 1550$ line in NGC 5548 (Kollatschny & Dietrich 1996). Another interpretation for the varying response might be off-axis variability (Gaskell & Goosmann 2013).

4.2. Vertical BLR structure in a sample of AGN

We deduced the BLR geometry of 3C 120 in Sect. 3.7 (see Fig. 23). Now we compare the spatial distribution of the line-emitting region in 3C 120 with those in other galaxies: NGC 7469, NGC 3783, NGC 5548, and 3C 390.3 (Kollatschny & Zetzl 2013c). We present in Fig. 24 the spatial distribution

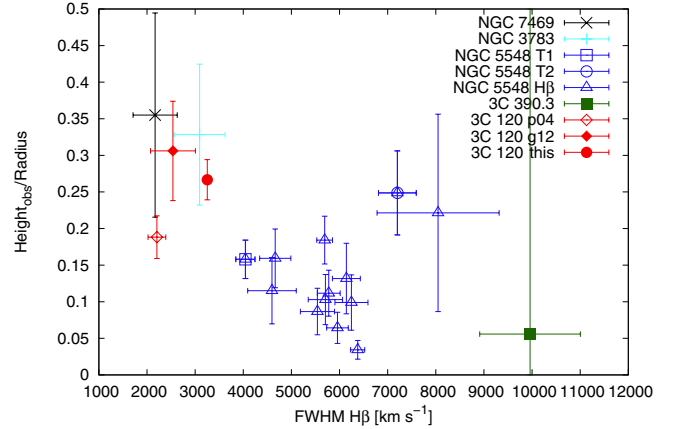


Fig. 25. Height-to-radius ratio for the $H\beta$ line-emitting regions of 3C 120 (red), NGC 7469 (black), NGC 3783 (cyan), NGC 5548 (blue), and 3C 390.3 (green).

of the line-emitting regions in 3C 120 (based on observations at three epochs) compared with NGC 5548 (two epochs for the highly ionized lines, 13 epochs for $H\beta$) and compared with NGC 7469, NGC 3783, and 3C 390.3 as a function of distance to the center and height above the midplane. The two axes scales in Fig. 24 are linear in units of light-days. We assumed that the accretion disk structures are arranged symmetrically to the midplane.

Different emission lines are highlighted by various colors and the different galaxies are marked by various symbols. The $H\beta$ emitting regions are drawn in red. The three $H\beta$ line-emitting regions of 3C 120 based on three different variability campaigns are connected by a dot-dashed red line and those of NGC 5548 (13 epochs) are connected by a solid red line. 3C 120 is the most luminous AGN. Therefore their radial $H\beta$ extension is largest for 3C 120 as expected (e.g. Kaspi et al. 2005). Different emission lines originate in different regions and at different distances from the center. The highly ionized (non-Balmer) lines of the individual galaxies are also connected by a solid line to illustrate general trends in the BLR structures of the different galaxies (see Kollatschny & Zetzl 2013c). The $H\beta$ emitting regions always originate closer to the midplane than the high-ionization lines. The line widths (with respect to the individual lines) control the height of the line-emitting regions above the midplane. NGC 7469 and 3C 120, for example, show the $H\beta$ profiles with the narrowest line widths. They originate at the largest distances above the midplane compared with the other AGN. Therefore, the broad emission-line regions are not simply scaled-up versions that only depend on the central luminosity (and central black hole mass).

To highlight this we show in Fig. 25 the height-to-radius ratio for the $H\beta$ line emitting regions in 3C 120, NGC 7469, NGC 3783, NGC 5548, and 3C 390.3 as a function of the $H\beta$ line width. This plot is based on the observed H/R values (Tables 10 and 1 in Kollatschny & Zetzl 2013b,c). The height-to-radius ratio for $H\beta$ is highest for galaxies with narrow emission lines and lowest for galaxies with broad lines. The overall picture we derived for the BLR region structure before in Kollatschny & Zetzl (2013c) is confirmed by the additional emission-line data of 3C 120.

5. Summary

We carried out a spectroscopic monitoring campaign of the Seyfert 1 galaxy 3C 120 with the 9.2 m HET, and in addition,

an accompanying photometric campaign with the WISE observatory in the years 2008 and 2009. The main results of our study can be summarized as follows:

1. The broad-line region is stratified compared with the line widths (FWHM) of the rms profiles, the variability amplitude of the emission lines, and the distance of the line-emitting regions from the center: the He II $\lambda 4686$ line originates closest to the center, the H α line originates farthest away. Based on these data – and without correcting for the contribution of turbulent velocity to the line profile – we derived a central black hole mass of $M = 10.8 \pm 2.6 \times 10^7 M_{\odot}$. Within the errors this is consistent with the black hole mass derived by Grier et al. (2012).
2. The velocity-delay maps of the H α and H β lines show a similar pattern as observations of H β made by Grier et al. (2013) one and a half years later. The emission line wings at distances of 2000 to 3000 km s⁻¹ from the line center respond much faster than the central region. The faster response of the line wings is explained by accretion disk models. In addition, these lines show a stronger response in their red wings. However, the velocity-delay maps of the He I $\lambda 5876$ and He II $\lambda 4686$ lines show a stronger response in the blue wing. Furthermore, the He II $\lambda 4686$ line responds faster in the blue wing in contradiction to the observations made one and a half years later when the galaxy was in a lower state. The faster response in the blue wing is an indication for central outflow motions when this galaxy was in a bright state during our observations.
3. The derived vertical BLR structure in 3C 120 coincides with that of other AGN. The general trend is confirmed: the emission lines of narrow-line AGN originate at larger distances from the midplane than AGN with broader emission lines.

Acknowledgements. This work has been supported by the DFG grants Ko 857/32-1 and HA 3555/12-1, and the Niedersachsen – Israel Research Cooperation Program ZN2318.

References

- Bentz, M. C., Walsh, J. L., Barth, A. J., et al. 2009, *ApJ*, 705, 199
 Bentz, M. C., Horne, K., Barth, A. J., et al. 2010, *ApJ*, 720, L46
 Burbidge, E. M. 1967, *ApJ*, 149, L51
 Chiang, J., & Murray, N. 1996, *ApJ*, 466, 704
 Crenshaw, D. M., Schmitt, H. R., Kraemer, S. B., et al. 2010, *ApJ*, 708, 419
 Denney, K. D., Peterson, B. M., Pogge, R. W., et al. 2009, *ApJ*, 704, L80
 Denney, K. D., Peterson, B. M., Pogge, R. W., et al. 2010, *ApJ*, 721, 715
 Dietrich, M., & Kollatschny, W. 1995, *A&A*, 303, 405
 French, H. B., & Miller, J. S. 1980, *PASP*, 92, 753
 Fromerth, M. J. & Melia, F. 2000, *ApJ*, 533, 172
 Gaskell, C. M. 1988, *ApJ*, 325, 114
 Gaskell, C. M. 2009, *New Astron. Rev.*, 53, 114
 Gaskell, C. M., & Goosmann, R. W. 2013, *ApJ*, 769, 30
 Gaskell, C. M., & Peterson, B. M. 1987, *ApJS*, 65,
 Grier, C. J., Peterson, B. M., Pogge, R. W., et al. 2012, *ApJ*, 755, 60
 Grier, C. J., Peterson, B. M., Horne, K., et al. 2013, *ApJ*, 764, 47
 Horne, K., Peterson, B. M., Collier, S. J., et al. 2004, *PASP*, 116, 465
 Kaspi, S., Maoz, D., Netzer, H., et al. 2005, *ApJ*, 629, 61
 Kollatschny, W. 2003, *A&A*, 407, 461
 Kollatschny, W., & Bischoff, K. 2002, *A&A*, 386, L19
 Kollatschny, W., & Dietrich, M. 1996, *A&A*, 314, 43
 Kollatschny, W., & Dietrich, M. 1997, *A&A*, 323, 5
 Kollatschny, W., & Zetzl, M. 2010, *A&A*, 522, A36
 Kollatschny, W., & Zetzl, M. 2011, *Nature*, 470, 366
 Kollatschny, W., & Zetzl, M. 2013a, *A&A*, 549, A100
 Kollatschny, W., & Zetzl, M. 2013b, *A&A*, 551, L6
 Kollatschny, W., & Zetzl, M. 2013c, *A&A*, 558, A26
 Kollatschny, W., Bischoff, K., Robinson, E. L., et al. 2001, *A&A*, 379, 125
 Koratkar, A., & Gaskell, M. 1991, *ApJ* 370, L61
 Korista, K. T., Alloin, D., Barr, P., et al. 1995, *ApJS*, 97, 285
 Netzer, H., Heller, A., Loinger, F., et al. 1996, *MNRAS*, 279, 429
 Oke, J. B., Readhead, A. C. S., & Sargent, W. L. W. 1980, *PASP*, 92, 758
 Perez, E., Robinson, A., & de la Fuente, L. 1992, *MNRAS*, 256, 103
 Peterson, B. M., Wanders, I., Bertram, R., et al. 1998, *ApJ*, 501, 82
 Peterson, B. M., Ferrarese, L., Gilbert, K. M., et al. 2004, *ApJ*, 613, 682
 Peterson, B. M., Denney, K. D., De Rosa, G., et al. 2013, *ApJ*, 779, 109
 Ramolla, M., Drass, H., Lemke, R., et al. 2013, *Astron. Nachr.*, 334, 1115
 Rodríguez-Pascual, P. M., Alloin, D., Clavel, J., et al. 1997, *ApJS*, 110, 9
 Welsh, W. F. 2001, in *Probing the Physics of AGN*, eds. B. M. Peterson et al., ASP Conf. Ser., 224, 123
 Welsh, W. F., & Horne, K. 1991, *ApJ*, 379, 586

Table 1. Log of spectroscopic observations of 3C 120 with HET.

Julian date 2 400 000+	UT date	Exp. time [s]
54 726.907	2008-09-17	1200.0
54 729.897	2008-09-20	1200.0
54 739.873	2008-09-30	600.0
54 740.870	2008-10-01	600.0
54 747.857	2008-10-08	600.0
54 748.847	2008-10-09	600.0
54 749.850	2008-10-10	600.0
54 752.834	2008-10-13	600.0
54 759.967	2008-10-20	600.0
54 762.815	2008-10-23	600.0
54 771.774	2008-11-01	600.0
54 775.771	2008-11-05	600.0
54 776.787	2008-11-06	600.0
54 779.773	2008-11-09	600.0
54 783.905	2008-11-13	600.0
54 787.745	2008-11-17	600.0
54 789.737	2008-11-19	1200.0
54 790.736	2008-11-20	600.0
54 793.723	2008-11-23	1200.0
54 807.681	2008-12-07	600.0
54 808.828	2008-12-08	600.0
54 822.652	2008-12-22	600.0
54 830.622	2008-12-30	600.0
54 841.600	2009-01-10	600.0
54 845.725	2009-01-14	600.0
54 866.691	2009-02-04	600.0
54 876.637	2009-02-14	600.0
54 881.635	2009-02-19	600.0
54 887.617	2009-02-25	600.0
54 893.604	2009-03-03	600.0
54 906.576	2009-03-16	600.0

Table 2. Log of photometric observations with the Wise and Cerro Armazones telescopes.

Julian date 2 400 000+	UT date	Filter
54 745.576	2008-10-06	V,R
54 745.584	2008-10-06	V,R
54 788.625	2008-11-18	I'
54 790.625	2008-11-20	I'
54 791.625	2008-11-21	I'
54 792.625	2008-11-22	I'
54 793.625	2008-11-23	I'
54 794.625	2008-11-24	I'
54 796.625	2008-11-26	I'
54 797.304	2008-11-26	V,R
54 797.625	2008-11-27	I'
54 798.625	2008-11-28	I'
54 799.625	2008-11-29	I'
54 800.625	2008-11-30	I'
54 802.625	2008-12-02	I'
54 803.297	2008-12-02	V,R
54 803.305	2008-12-02	V,R
54 803.625	2008-12-03	I'
54 804.304	2008-12-03	V,R
54 804.312	2008-12-03	V,R
54 804.322	2008-12-03	V,R
54 804.331	2008-12-03	V,R
54 804.625	2008-12-04	I'
54 805.296	2008-12-04	V,R
54 805.303	2008-12-04	V,R
54 805.331	2008-12-04	V,R
54 808.342	2008-12-04	V,R
54 808.350	2008-12-04	V,R
54 808.357	2008-12-04	V,R
54 811.327	2008-12-10	V,R
54 817.282	2008-12-16	V,R
54 817.508	2008-12-16	V,R
54 818.289	2008-12-17	V,R
54 819.297	2008-12-18	V,R
54 825.353	2008-12-24	V,R
54 826.432	2008-12-25	V,R
54 837.205	2009-01-05	V,R
54 837.213	2009-01-05	V,R
54 838.203	2009-01-06	V,R
54 839.332	2009-01-07	V,R
54 841.600	2009-01-10	V,R
54 852.172	2009-01-20	V,R
54 853.170	2009-01-21	V,R
54 856.201	2009-01-24	V,R
54 859.178	2009-01-27	V,R
54 866.192	2009-02-03	V,R
54 867.180	2009-02-04	V,R
54 893.604	2009-03-03	V,R
54 894.191	2009-03-03	V,R
54 895.192	2009-03-04	V,R
54 903.304	2009-03-12	V,R
54 905.205	2009-03-14	V,R
54 908.238	2009-03-17	V,R
54 920.215	2009-03-29	V,R
55 064.527	2009-08-21	V,R
55 064.535	2009-08-21	V,R
55 098.571	2009-09-24	V,R
55 117.533	2009-10-13	V,R

Table 4. Continuum and integrated broad-line fluxes for different epochs.

Julian date 2 450 000+	Cont. 5100 Å	H α	H β	H γ	He I	He II
(1)	(2)	(3)	(4)	(5)	(6)	(7)
4726.907	4.045 ± 0.099	26.23 ± 0.62	5.21 ± 0.08	1.95 ± 0.03	1.71 ± 0.04	1.12 ± 0.02
4729.897	4.300 ± 0.038	25.36 ± 0.71	5.49 ± 0.05	1.74 ± 0.01	1.67 ± 0.05	1.08 ± 0.01
4739.873	4.187 ± 0.278	24.71 ± 2.29	5.01 ± 0.32	2.18 ± 0.14	1.49 ± 0.14	0.76 ± 0.05
4740.870	3.891 ± 0.030	22.62 ± 0.73	4.62 ± 0.06	1.53 ± 0.02	1.46 ± 0.05	1.08 ± 0.01
4747.857	4.345 ± 0.033	26.48 ± 0.44	5.47 ± 0.07	1.81 ± 0.02	1.77 ± 0.03	1.17 ± 0.01
4748.847	4.117 ± 0.035	25.19 ± 0.37	5.12 ± 0.05	1.70 ± 0.02	1.64 ± 0.02	1.10 ± 0.01
4749.850	4.229 ± 0.043	25.59 ± 0.36	5.30 ± 0.03	1.74 ± 0.01	1.68 ± 0.02	1.13 ± 0.01
4752.834	4.381 ± 0.057	25.46 ± 0.93	5.52 ± 0.06	1.77 ± 0.02	1.73 ± 0.06	1.07 ± 0.01
4759.967	4.318 ± 0.040	24.86 ± 0.52	5.41 ± 0.07	1.75 ± 0.02	1.66 ± 0.04	1.04 ± 0.01
4762.815	3.790 ± 0.265	23.35 ± 2.20	4.81 ± 0.42	1.82 ± 0.16	1.49 ± 0.14	0.79 ± 0.07
4771.774	4.219 ± 0.080	23.43 ± 0.47	4.78 ± 0.14	1.79 ± 0.05	1.40 ± 0.03	0.77 ± 0.02
4775.771	4.445 ± 0.026	25.25 ± 0.49	4.92 ± 0.03	1.62 ± 0.01	1.67 ± 0.03	0.90 ± 0.01
4776.787	4.272 ± 0.044	24.95 ± 0.46	4.81 ± 0.06	1.55 ± 0.02	1.66 ± 0.03	0.91 ± 0.01
4779.773	4.660 ± 0.045	26.21 ± 0.57	5.18 ± 0.07	1.62 ± 0.02	1.75 ± 0.04	0.93 ± 0.01
4783.905	4.297 ± 0.037	24.17 ± 0.70	4.72 ± 0.03	1.44 ± 0.01	1.64 ± 0.05	0.98 ± 0.01
4787.745	4.918 ± 0.045	25.88 ± 0.36	5.11 ± 0.03	1.59 ± 0.01	1.73 ± 0.02	0.93 ± 0.01
4789.737	5.065 ± 0.274	25.13 ± 1.74	5.08 ± 0.30	1.51 ± 0.09	1.76 ± 0.12	1.00 ± 0.06
4790.736	5.052 ± 0.033	25.76 ± 0.66	4.91 ± 0.03	1.56 ± 0.01	1.68 ± 0.04	0.90 ± 0.01
4793.723	5.073 ± 0.034	24.46 ± 0.34	4.92 ± 0.01	1.60 ± 0.01	1.60 ± 0.02	1.15 ± 0.01
4807.681	5.819 ± 0.311	26.28 ± 1.81	5.39 ± 0.30	1.81 ± 0.10	1.81 ± 0.12	1.65 ± 0.09
4808.828	5.615 ± 0.043	24.73 ± 0.56	5.58 ± 0.05	2.49 ± 0.02	1.70 ± 0.04	2.16 ± 0.02
4822.652	4.824 ± 0.039	22.69 ± 0.74	5.16 ± 0.16	2.29 ± 0.05	1.71 ± 0.06	1.79 ± 0.04
4830.622	4.859 ± 0.060	25.62 ± 0.66	5.83 ± 0.10	2.59 ± 0.04	1.82 ± 0.05	1.72 ± 0.03
4841.600	4.910 ± 0.040	25.59 ± 0.47	5.99 ± 0.06	2.67 ± 0.03	1.84 ± 0.03	1.65 ± 0.02
4845.725	4.532 ± 0.041	24.02 ± 0.63	5.28 ± 0.05	2.19 ± 0.02	1.67 ± 0.04	1.39 ± 0.01
4866.691	4.261 ± 0.257	21.74 ± 1.54	4.88 ± 0.29	2.06 ± 0.12	1.54 ± 0.11	1.43 ± 0.09
4876.637	4.829 ± 0.085	24.77 ± 0.90	5.51 ± 0.12	2.37 ± 0.05	1.65 ± 0.05	1.75 ± 0.04
4881.635	5.061 ± 0.025	25.31 ± 0.55	5.97 ± 0.09	2.52 ± 0.04	1.74 ± 0.04	1.88 ± 0.03
4887.617	4.916 ± 0.036	25.74 ± 0.53	5.59 ± 0.10	1.79 ± 0.03	1.78 ± 0.04	1.35 ± 0.02
4893.604	4.722 ± 0.043	25.46 ± 0.55	5.79 ± 0.05	2.09 ± 0.02	1.69 ± 0.04	1.45 ± 0.01
4906.576	3.807 ± 0.036	23.49 ± 0.39	5.23 ± 0.07	1.82 ± 0.02	1.67 ± 0.03	1.00 ± 0.01

Notes. Continuum flux (2) in units of 10^{-15} erg s $^{-1}$ cm $^{-2}$ Å $^{-1}$. Line fluxes (3)–(7) in units 10^{-13} erg s $^{-1}$ cm $^{-2}$.

Table 5. Continuum fluxes at 5100 Å (*V*-band) and 6170 Å (*R*-band) taken with the HET (H), Wise (W), and Cerro Armazones (C) telescopes at different epochs.

Julian date 2 450 000+	Cont. flux 5100 Å	Julian date 2 450 000+	Cont. flux 6200 Å	Telescope
4726.907	4.045 ± 0.099	4726.907	4.158 ± 0.056	H
4729.897	4.300 ± 0.038	4729.897	3.967 ± 0.035	H
4739.873	4.187 ± 0.278	4739.873	4.076 ± 0.287	H
4740.870	3.891 ± 0.030	4740.870	3.765 ± 0.044	H
4745.580	4.129 ± 0.111	4745.576	3.848 ± 0.099	W
4745.588	4.163 ± 0.104	4745.584	3.805 ± 0.095	W
4747.857	4.345 ± 0.033	4747.857	4.161 ± 0.029	H
4748.847	4.117 ± 0.035	4748.847	3.958 ± 0.030	H
4749.850	4.229 ± 0.043	4749.850	4.004 ± 0.026	H
4752.834	4.381 ± 0.057	4752.834	3.951 ± 0.029	H
4759.967	4.318 ± 0.040	4759.967	3.907 ± 0.045	H
4762.815	3.790 ± 0.265	4762.815	3.716 ± 0.266	H
4771.774	4.219 ± 0.080	4771.774	4.084 ± 0.076	H
4775.771	4.445 ± 0.026	4775.771	4.176 ± 0.031	H
4776.787	4.272 ± 0.044	4776.787	4.106 ± 0.028	H
4779.773	4.660 ± 0.045	4779.773	4.337 ± 0.033	H
4783.905	4.297 ± 0.037	4783.905	4.083 ± 0.052	H
4787.745	4.918 ± 0.045	4787.745	4.464 ± 0.030	H
		4788.625	4.406 ± 0.088	C
4789.737	5.065 ± 0.274	4789.737	4.514 ± 0.250	H
		4790.625	4.470 ± 0.094	C
4790.736	5.052 ± 0.033	4790.736	4.589 ± 0.051	H
		4791.625	4.488 ± 0.096	C
		4792.625	4.455 ± 0.093	C
		4793.625	4.456 ± 0.093	C
4793.723	5.073 ± 0.034	4793.723	4.431 ± 0.031	H
		4794.625	4.539 ± 0.101	C
		4796.625	4.504 ± 0.098	C
4797.308	5.220 ± 0.118	4797.304	4.456 ± 0.111	W
		4797.625	4.442 ± 0.092	C
		4798.625	4.505 ± 0.098	C
		4799.625	4.532 ± 0.101	C
		4800.625	4.510 ± 0.099	C
		4802.625	4.505 ± 0.098	C
4803.301	5.597 ± 0.129	4803.297	4.798 ± 0.096	W
4803.309	5.562 ± 0.122	4803.305	4.767 ± 0.101	W
		4803.625	4.528 ± 0.100	C
4804.308	5.486 ± 0.151	4804.304	4.655 ± 0.113	W
4804.315	5.513 ± 0.148	4804.312	4.643 ± 0.116	W
4804.326	5.507 ± 0.152	4804.322	4.692 ± 0.121	W
		4804.331	4.705 ± 0.114	W
		4804.625	4.557 ± 0.103	C
4805.299	5.633 ± 0.121	4805.296	4.792 ± 0.104	W
4805.307	5.604 ± 0.136	4805.303	4.817 ± 0.105	W
4805.335	5.562 ± 0.135	4805.331	4.730 ± 0.103	W
4807.681	5.819 ± 0.311	4807.681	5.068 ± 0.289	H
4808.346	5.500 ± 0.124	4808.342	4.855 ± 0.103	W
4808.354	5.689 ± 0.131	4808.350	4.887 ± 0.119	W
4808.361	5.486 ± 0.130	4808.357	4.849 ± 0.100	W
4808.828	5.615 ± 0.043	4808.828	4.866 ± 0.040	H
4811.331	5.725 ± 0.683	4811.327	4.983 ± 0.870	W
4817.286	5.640 ± 0.159	4817.282	5.074 ± 0.127	W
4817.512	5.576 ± 0.178	4817.508	5.022 ± 0.140	W
4818.293	5.437 ± 0.154	4818.289	4.874 ± 0.163	W
4819.301	5.362 ± 0.121	4819.297	4.680 ± 0.099	W
4822.652	4.824 ± 0.039	4822.652	4.466 ± 0.034	H
		4825.353	4.944 ± 0.131	W
		4826.432	4.849 ± 0.115	W
4830.622	4.859 ± 0.060	4830.622	4.615 ± 0.047	H
4837.209	4.600 ± 0.147	4837.205	4.245 ± 0.128	W
4837.217	4.687 ± 0.165	4837.213	4.176 ± 0.120	W
		4838.203	4.408 ± 0.216	W

Notes. Continuum flux in units of 10^{-15} erg s $^{-1}$ cm $^{-2}$ Å $^{-1}$.

Table 5. continued.

Julian date 2 450 000+	Cont. flux 5100 Å	Julian date 2 450 000+	Cont. flux 6200 Å	Telescope
4839.335	4.849 ± 0.349	4839.332	4.396 ± 0.252	W
4841.600	4.910 ± 0.040	4841.600	4.524 ± 0.024	H
4845.725	4.532 ± 0.041	4845.725	4.284 ± 0.032	H
4852.176	5.003 ± 0.118	4852.172	4.332 ± 0.105	W
4853.174	4.786 ± 0.119	4853.170	4.181 ± 0.096	W
4856.205	5.281 ± 0.135	4856.201	4.680 ± 0.108	W
4859.182	4.856 ± 0.118	4859.178	4.227 ± 0.109	W
4866.195	4.805 ± 0.269	4866.192	4.268 ± 0.172	W
4866.691	4.261 ± 0.257	4866.691	3.951 ± 0.225	H
4867.184	4.749 ± 0.186	4867.180	4.216 ± 0.226	W
4876.637	4.829 ± 0.085	4876.637	4.435 ± 0.091	H
4881.635	5.061 ± 0.025	4881.635	4.422 ± 0.038	H
4887.617	4.916 ± 0.036	4887.617	4.336 ± 0.029	H
4893.604	4.722 ± 0.043	4893.604	4.337 ± 0.032	H
4894.195	4.426 ± 0.122	4894.191	4.035 ± 0.095	W
4895.196	4.366 ± 0.114	4895.192	3.952 ± 0.110	W
		4903.304	3.974 ± 0.184	W
4905.209	3.939 ± 0.106	4905.205	3.667 ± 0.087	W
4906.576	3.807 ± 0.036	4906.576	3.687 ± 0.047	H
4908.242	3.884 ± 0.094	4908.238	3.704 ± 0.083	W
4920.219	3.681 ± 0.087	4920.215	3.482 ± 0.076	W
5064.531	2.944 ± 0.081	5064.527	2.737 ± 0.074	W
5064.538	2.912 ± 0.082	5064.535	2.768 ± 0.073	W
5098.574	2.386 ± 0.098	5098.571	2.395 ± 0.076	W
5117.536	2.953 ± 0.088	5117.533	2.599 ± 0.075	W